Commun. Comput. Phys.
doi: 10.4208/cicp.OA-2022-0052

Vol. **33**, No. 1, pp. 101-117
January 2023

A Characteristic Boundary Condition for Multispeed Lattice Boltzmann Methods

Friedemann Klass[1,*], Alessandro Gabbana[2] and Andreas Bartel[1]

[1] *University of Wuppertal, Gaußstraße 20, 42119 Wuppertal, Germany.*
[2] *Eindhoven University of Technology, 5600 MB Eindhoven, The Netherlands.*

Received 19 February 2022; Accepted (in revised version) 1 July 2022

Abstract. We present the development of a non-reflecting boundary condition, based on the Local One-Dimensional Inviscid (LODI) approach, for Lattice Boltzmann Models working with multi-speed stencils.
We test and evaluate the LODI implementation with numerical benchmarks, showing significant accuracy gains with respect to the results produced by a simple zero-gradient condition. We also implement a simplified approach, which allows handling the unknown distribution functions spanning several layers of nodes in a unified way, still preserving a comparable level of accuracy with respect to the standard formulation.

AMS subject classifications: 76M28, 76P05, 76M20

Key words: Characteristic boundary condition, non-reflective boundary conditions, local one-dimensional inviscid boundary conditions, lattice Boltzmann method, multispeed high order models.

1 Introduction

The Lattice Boltzmann Method (LBM) has emerged in the past decades as a computationally efficient fluid dynamic solver [1]. Originally developed for the simulation of isothermal weakly compressible flows, over the years several works have described possible approaches for extending the applicability of the method [2]. A possible pathway is offered by models based on higher order Gauss-Hermite quadrature [3–5], which in turn require the adoption of a discretization of the velocity space by means of multi-speed stencils. This approach has been successfully employed in the definition of LBM models for the study of, among others, compressible flows [3,6–8], rarefied gas flows [9–11] flows in curved space [12], semi-classic fluids [13] and relativistic flows [14].

*Corresponding author. *Email addresses:* Friedemann.Klass@math.uni-wuppertal.de (F. Klass), a.gabbana@tue.nl (A. Gabbana), Andreas.Bartel@math.uni-wuppertal.de (A. Bartel)

However, the presence of multiple speed levels introduces complications in the definition of accurate Boundary Conditions (BC). There is not much literature available in relationship to the development of boundary conditions for multi-speed LBM, with few examples of implementation of Dirichlet BC [15, 16], diffusive BC [17], and the so called Tamm-Moth-Smith BC, specially devised for handling shock waves [7].

In this work, we take into consideration artificial BC, which are commonly employed for restricting a large, or even unbounded, physical domain to a (smaller) feasible computational domain. Ideally, the application of this class of BC should be such not to introduce spurious artifacts in the bulk dynamics. In particular, the BC should not cause reflections of pressure waves.

This type of setup is commonly modeled by employing a class of BC going under the name of Non-Reflecting BC (NRBC). A few examples are given by i) the perfectly matched layer technique [18], where a damping layer is attached to the computational domain, ii) the discrete artificial boundary condition [19], where the information entering the computational domain is approximated using another LBM simulation and iii) characteristic boundary conditions, where wave amplitude variations are manipulated (e.g. [20]). In this work we focus on this latter approach.

Based on the work by Hedstrom [21], Thompson [22] established characteristic boundary conditions for nonlinear hyperbolic systems such as the Euler equations. The general idea is to decompose information at the boundary into characteristic waves. The variation of the outgoing wave amplitude can be then computed from the adjacent fluid nodes, whereas incoming waves need to be specified using (application dependent) external information. This approach has been applied to non-hyperbolic Navier-Stokes equations by Poinsot and Lele [23]. In their work, the wave amplitude variations are approximated using the one-dimensional Euler equations. Dropping the transversal and viscous terms, this is referred to as a Local one-dimensional inviscid (LODI) problem.

The LODI procedure has been applied to single-speed LBM [20]. Thereby, macroscopic values obtained from the LODI problem are used to specify a Dirichlet condition in LBM simulations.

In this work, we extend the approach described in [20] to multi-speed models. We restrict our analysis to iso-thermal weakly compressible flows, in what can be seen as a first step towards the definition of a characteristic BC for high-order LBM capable of handling more complex flows.

This article is structured as follows: in Section 2 we provide a brief description of the multi-speed LBM used in this work. In Section 3, we give the mathematical formulation of the LODI framework, and introduce the extension to the multi-speed setting. We numerically evaluate the accuracy of this boundary condition for two benchmark cases, reporting the results in Section 4. Concluding remarks and future directions are summarized in Section 5.

2 The lattice Boltzmann method

In this section, we provide a short introduction to the LBM (the reader is referred to [1] for a more thorough introduction).

The LBM framework is set at the mesoscopic level, with the fluid described in terms of discrete probability distribution functions $f_i(\mathbf{x},t)$, to which we will refer to, in what follows, as "populations". For each grid point $\mathbf{x}$, populations are associated to a fixed set of discrete velocities $\mathbf{c}_i$, $i=1,\cdots,q$. It is customary to refer to different velocity sets using the DdQq nomenclature, where d represents the spatial dimension and q the number of discrete velocity components. The discrete velocities are chosen to coincide with the abscissa of a Gauss-Hermite quadrature $\{(\omega_i,\mathbf{c}_i) : i=1,\cdots,q\}$ with weights ω_i. In this work, we consider the D2Q17 model (see Fig. 1), which is compatible with a seventh-order quadrature rule [5,24]. Its weights are given in Table 1.

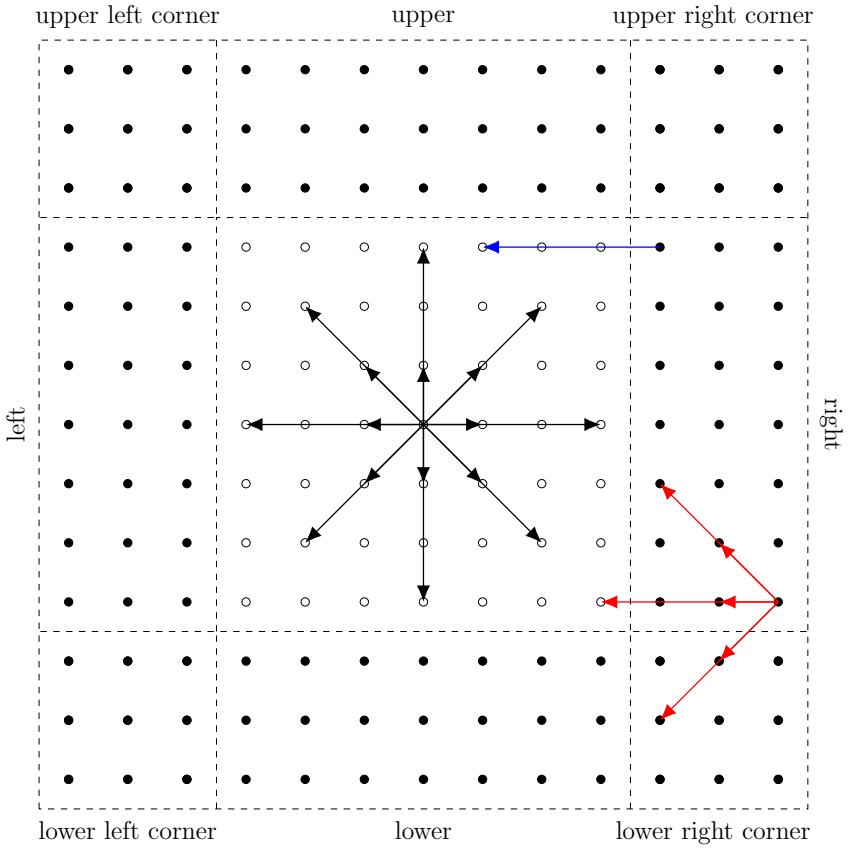

Figure 1: Sketch of the computational domain used in this work. We use the D2Q17 model, for which the stencil is depicted in the center of the domain. Hollow (filled) nodes represent fluid (boundary) nodes. The red arrows provide an example of lattice populations for which boundary conditions need to be specified in the outermost layer, with blue arrows giving an example in the innermost layer.

Table 1: Lattice weights of the D2Q17 model. Each velocity $\mathbf{c}_i$ is associated with the weight $\omega_{\mathbf{c}_i\cdot\mathbf{c}_i+1}$.

weight	value
ω_1	0.4020051469091126
ω_2	0.1161548664977815
ω_3	0.0330063536229869
ω_4	0.0002584145497874
ω_5	0.0000790786021659

The time evolution of each lattice population is ruled by the discrete lattice Boltzmann equation, here is the single relaxation time approximation [25]:

$$f_i(\mathbf{x}+\mathbf{c}_i\Delta t,t+\Delta t)=f_i(\mathbf{x},t)-\frac{\Delta t}{\tau}\left(f_i(\mathbf{x},t)-f_i^{\mathrm{eq}}(\mathbf{x},t)\right), \tag{2.1}$$

where Δt is the time step, τ the relaxation time, and f_i^{eq} is the discrete equilibrium distribution function, for which we take a third order expansion in Hermite polynomials [26]:

$$f_i^{\mathrm{eq}}(\rho,\mathbf{u})=\omega_i\rho\left(1+\mathbf{u}\cdot\mathbf{c}_i+\frac{1}{2c_s^2}\left[(\mathbf{u}\cdot\mathbf{c}_i)^2-u^2\right]+\frac{\mathbf{u}\cdot\mathbf{c}_i}{6c_s^4}\left[(\mathbf{u}\cdot\mathbf{c}_i)^2-3u^2\right]\right), \tag{2.2}$$

where ρ and $\mathbf{u}$ are macroscopic density and velocity respectively, $u^2=\mathbf{u}\cdot\mathbf{u}$ and c_s denotes the lattice speed of sound.

The right hand side of Eq. (2.1) is commonly referred to as the collision step. Here, the interaction of respective populations at each grid point is modeled as a relaxation with rate τ towards an equilibrium state given by (2.2). At the left hand side of Eq. (2.1), these post-collisional populations are moved to neighboring nodes along the directions $\mathbf{c}_i$ defined by the stencil.

The macroscopic density ρ and velocity $\mathbf{u}$ are calculated form the velocity moments of the particle distribution function. Thanks to the underlying quadrature rule, they can be expressed in terms of discrete summations over the lattice populations:

$$\rho=\sum_{i=1}^{q}f_i,\quad \rho\mathbf{u}=\sum_{i=1}^{q}f_i\mathbf{c}_i. \tag{2.3}$$

By applying a multiscale Chapman-Enskog expansion [27], it can be shown that Eq. (2.1) provides a second order approximation of the macroscopic Navier-Stokes equations:

$$\frac{\partial\rho}{\partial t}+\nabla\cdot(\rho\mathbf{u})=0,\quad \frac{\partial\rho\mathbf{u}}{\partial t}+\nabla\cdot\left(\rho\mathbf{u}\cdot\mathbf{u}^{\top}\right)=-c_s^2\nabla\rho+\nabla\cdot\sigma, \tag{2.4}$$

with the following relationship between the kinematic viscosity ν of the fluid and the relaxation time parameter τ:

$$\nu=\left(\tau-\frac{1}{2}\right)c_s^2. \tag{2.5}$$

3 The LODI BC

In this section, we define the LODI mathematical framework in a $d=2$ dimensional domain. We then extend the LODI BC established for the D2Q9 stencil [28] to multi-speed models.

3.1 Characteristic analysis

Starting form the Navier-Stokes equations (2.4), we drop the deviatoric stress

$$\nabla\cdot\sigma=\nabla\cdot\mu\left[\nabla\mathbf{u}+\nabla\mathbf{u}^{\top}-\frac{2}{d}(\nabla\cdot\mathbf{u})\mathbf{I}\right]=\mu\begin{bmatrix}\frac{\partial^2}{\partial x^2}u_x+\frac{\partial^2}{\partial y^2}u_x\\ \frac{\partial^2}{\partial y^2}u_y+\frac{\partial^2}{\partial x^2}u_y\end{bmatrix}, \tag{3.1}$$

in order to obtain a hyperbolic system in the unknowns $U=\left(\rho,u_x,u_y\right)^{\top}$:

$$\frac{\partial U}{\partial t}+A\frac{\partial U}{\partial x}+B\frac{\partial U}{\partial y}=0,\quad \text{with}\quad A=\begin{pmatrix}u_x & \rho & 0\\ \frac{c_s^2}{\rho} & u_x & 0\\ 0 & 0 & u_x\end{pmatrix},\quad B=\begin{pmatrix}u_y & 0 & \rho\\ 0 & u_y & 0\\ \frac{c_s^2}{\rho} & 0 & u_y\end{pmatrix}. \tag{3.2}$$

The matrices A and B are similar to diagonal matrices $\Lambda=\text{diag}(u_x-c_s,u_x,u_x+c_s)$ and $V=\text{diag}(u_y-c_s,u_y,u_y+c_s)$ respectively [22,28]:

$$\Lambda=SAS^{-1},\quad \text{with}\quad S=\begin{pmatrix}c_s^2 & -c_s\rho & 0\\ 0 & 0 & 1\\ c_s^2 & c_s\rho & 0\end{pmatrix},\quad S^{-1}=\begin{pmatrix}\frac{1}{2c_s^2} & 0 & \frac{1}{2c_s^2}\\ -\frac{1}{2c_s\rho} & 0 & \frac{1}{2c_s\rho}\\ 0 & 1 & 0\end{pmatrix},$$

$$V=TBT^{-1},\quad \text{with}\quad T=\begin{pmatrix}c_s^2 & 0 & -c_s\rho\\ 0 & 1 & 0\\ c_s^2 & 0 & c_s\rho\end{pmatrix},\quad T^{-1}=\begin{pmatrix}\frac{1}{2c_s^2} & 0 & \frac{1}{2c_s^2}\\ 0 & 1 & 0\\ -\frac{1}{2c_s\rho} & 0 & \frac{1}{2c_s\rho}\end{pmatrix}.$$

We now rewrite the spatial derivatives in the direction normal to the boundary as

$$A\frac{\partial U}{\partial x}=S^{-1}\Lambda S\frac{\partial U}{\partial x}=:S^{-1}\mathcal{L}_x.$$

In the above, the term $\mathcal{L}_x$ describes the amplitude variations of the characteristic waves, and can be expressed as

$$\mathcal{L}_x=\begin{pmatrix}\mathcal{L}_{x,1}\\ \mathcal{L}_{x,2}\\ \mathcal{L}_{x,3}\end{pmatrix}=\begin{pmatrix}(u_x-c_s)(c_s^2\frac{\partial\rho}{\partial x}-c_s\rho\frac{\partial u_x}{\partial x})\\ u_x\frac{\partial u_y}{\partial x}\\ (u_x+c_s)(c_s^2\frac{\partial\rho}{\partial x}+c_s\rho\frac{\partial u_x}{\partial x})\end{pmatrix}. \tag{3.3}$$

This formulation allows distinguishing between incoming and outgoing waves, on the basis of the sign of the eigenvalues [22]. The i-th characteristic wave with amplitude variation $\mathcal{L}_{x,i}$ travels in positive (negative) x-direction if $\Lambda_{i,i}$ is positive (negative). Moreover, amplitude variations of outgoing waves can be computed from the bulk dynamics. We now describe how this information can be used to formulate a BC.

3.2 LODI BC for straight boundaries

The amplitude variations of incoming waves can be modeled in several ways: They may be i) set to zero to pose a perfectly non-reflecting BC, ii) computed from an imposed macroscopic value or iii) computed from a relaxation towards such a desired value [29]. We refer to [30] and references therein for more details. Here, we stick to annihilating incoming waves by setting their amplitude variations to zero, i.e., we substitute $\mathcal{L}_x$ with

$$\bar{\mathcal{L}}_{x,i} = \begin{cases} \mathcal{L}_{x,i}, & \text{outgoing wave,} \\ 0, & \text{incoming wave.} \end{cases} \tag{3.4}$$

In the LODI framework, only the direction normal to the boundary is considered. For example, considering a right boundary (cf. Fig. 1), we set $\frac{\partial U}{\partial y} \equiv 0$, and therefore Eq. (3.2) becomes

$$\frac{\partial U}{\partial t} = -S^{-1}\bar{\mathcal{L}}_x = \begin{pmatrix} -\frac{1}{2c_s^2}\left(\bar{\mathcal{L}}_{x,1}+\bar{\mathcal{L}}_{x,3}\right) \\ \frac{1}{2\rho c_s}\left(\bar{\mathcal{L}}_{x,1}-\bar{\mathcal{L}}_{x,3}\right) \\ -\bar{\mathcal{L}}_{x,2} \end{pmatrix}. \tag{3.5}$$

The solution of the above system of equations, calculated at boundary node $\mathbf{x}_b$, allows determining the macroscopic target values to be imposed at the boundary. One can do so, for example, by imposing the equilibrium distribution calculated using the target macroscopic values for the boundary nodes, or with other approaches allowing to implement a Dirichlet BC for multi-speed LBM [15, 16].

Since the D2Q17 velocity stencil exhibits a maximum displacement of $M=3$, we need to treat several layers of nodes with the procedure outlined above. Letting Z represent a generic macroscopic quantity and $\mathbf{e}_x$ the normal unit vector in x-direction, the spatial discretization of Eq. (3.5) is performed using one sided finite differences

$$\frac{\partial Z(\mathbf{x}_b,t)}{\partial x} \approx -\frac{1}{2}\left(-3Z(\mathbf{x}_b,t)+4Z(\mathbf{x}_b-\mathbf{e}_x,t)-Z(\mathbf{x}_b-2\mathbf{e}_x,t)\right) \tag{3.6}$$

at the outermost layers of boundary nodes and central finite differences

$$\frac{\partial Z(\mathbf{x}_b,t)}{\partial x} \approx \frac{1}{2}\left(Z(\mathbf{x}_b+\mathbf{e}_x,t)-Z(\mathbf{x}_b-\mathbf{e}_x,t)\right) \tag{3.7}$$

at the inner nodes. The time integration of Eq. (3.5) is performed using a simple Euler step.

3.3 Zero-gradient LODI

The treatment of several layers of boundary nodes in a multi-speed setting can be simplified by employing a unified approach [15], where nodes belonging to different layers are subjected to identical macroscopic values.

Therefore, we introduce here a simplified version of the LODI BC, where we apply the procedure defined in the previous section only to the innermost layer of boundary nodes, in order to define the target macroscopic values which will be same for all different layers. This de-facto corresponds to applying a zero gradient LODI BC. Hereafter, we refer to this implementation with the label LZG.

We summarize the working principle of both these implementations for the case of a right boundary in a pseudocode in the appendix.

3.4 Treatment of corners

For the treatment of corners, both x- and y-directions are considered normal to the wall [22]. We consider, for example, the lower/upper right corner depicted in Fig. 1. In this case, we have to take into account all spatial derivatives appearing in Eq. (3.2):

$$B\frac{\partial U}{\partial y} = T^{-1}VT\frac{\partial U}{\partial y} =: T^{-1}\mathcal{L}_y.$$

Consequently, Eq. (3.2) becomes

$$\frac{\partial U}{\partial t} = -S^{-1}\bar{\mathcal{L}}_x - T^{-1}\bar{\mathcal{L}}_y,$$

where $\bar{\mathcal{L}}_y$ is defined analogously to $\bar{\mathcal{L}}_x$.

For the LODI BC, the above equation is solved for each of the M^2 nodes forming the corner. In the LZG scheme, only the corner node adjacent to a fluid node is considered in the calculation of the target macroscopic values, which are then imposed to all remaining corner nodes.

4 Numerical results

In this section, we evaluate the accuracy of the BC defined in Section 3 for two different benchmarks. In order to quantify the accuracy of each BC, we calculate the relative L^2-error e_Z for a generic macroscopic field $Z \in \{\rho, u_x, u_y\}$ with respect to a reference field Z^{ref} as

$$e_Z = \sqrt{\frac{\sum_{i=1}^{L_x}\sum_{j=1}^{L_y}\left(Z^{\text{ref}}(x_i,y_j) - Z^{\text{sim}}(x_i,y_j)\right)^2}{\sum_{i=1}^{L_x}\sum_{j=1}^{L_y}\left(Z^{\text{ref}}(x_i,y_j)\right)^2}}.$$

The reference fields Z^{ref} are obtained from a fully periodic LBM simulation on an extended grid. In particular, the reference simulation makes use of a sufficiently large grid such that no interaction takes place between the boundaries and the bulk dynamics of a (smaller) computational domain that we use as ground truth.

In order to put our analysis into perspective, we compare the LODI and the LZG BCs with a zero gradient BC (ZG in what follows), defined such to set to zero the gradients of macroscopic fields normal in the direction normal to the boundary:

$$f_i(\mathbf{x}_f + k\mathbf{n}, t) = f_i^{\text{eq}}(\mathbf{x}_f, t-1), \quad k = 1, \cdots, M$$

with $\mathbf{x}_f$ a fluid node adjacent to a boundary, and with $\mathbf{n}$ the outward normal unit vector with respect to the wall.

4.1 Density perturbation

We start our analysis by considering a strictly mono-dimensional dynamics originating from the following initial conditions for density and velocity:

$$\begin{aligned}\rho(x,y) &= \bar{\rho} + \frac{\bar{\rho}-\rho_0}{2}\left(\tanh\left(\mathrm{s}\left(x-\tfrac{L_x}{2}\right)\right)-1\right),\\ \mathbf{u}(x,y) &= (\mathrm{Ma}\cdot c_s, 0)\end{aligned}$$

with $\bar{\rho}=1.005$, $\rho_0=1$ and steepness parameter $\mathrm{s}=0.5$. The Mach number is $\mathrm{Ma}=0.05$ and the relaxation time used in simulation was $\tau=0.9$ in numerical units. We use a grid of size $L_x \times L_y = 100 \times 50$, and apply periodic boundary conditions on top and bottom walls, while left and right boundaries are equipped with artificial BC.

The resulting flow was evolved for $N_{iter}=1000$ time steps. The fully periodic reference simulation took place on a $\hat{L}_x \times L_y$ grid, where $\hat{L}_x = L_x + 2MN_{iter}$. That is, the domain of interest has been extended by MN_{iter} layers of nodes to the left and right respectively to ensure no information re-enters in the given amount of time steps.

In the reference simulation, the macroscopic fields within the domain of interest (i.e. used in the comparison) reach a plateau value as soon as the initial perturbation has traveled sufficiently far from the center of the grid. This occurs after about 150 time steps.

When working on the truncated domain, artificial BC introduce spurious reflection waves, which depending on the level of accuracy of the chosen BC implementation may lead to steady state solutions with significant departures from the ground truth.

In Fig. 2 we show the time evolution of the relative L^2-errors e_ρ and e_{u_x} for the three different type of BC implemented. We observe that in all three cases, the value of the error rise up to a peak during the initial stages, as the wave starts interacting with the boundaries. During this initial phase, the LODI scheme consistently outperforms both the ZG and the LZG.

After about 100 time steps, the errors caused by LODI and LZG almost coincide. The unphysical reflections caused at the each x-boundary proceed to travel through the bulk

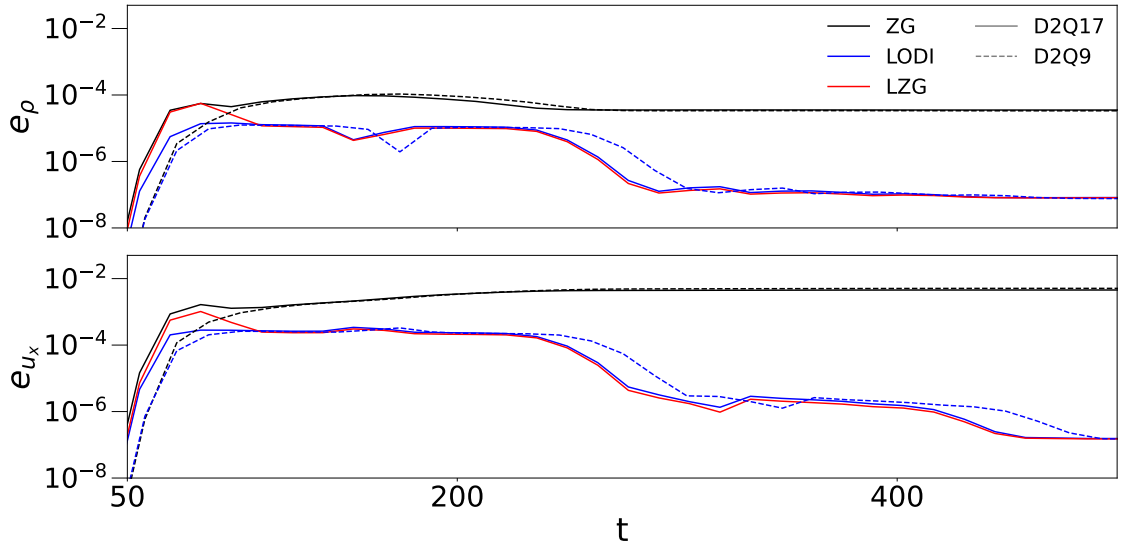

Figure 2: Time evolution of e_ρ and e_{u_x}. Solid (dashed) lines correspond to simulations using the D2Q17 (D2Q9) velocity stencil. For both stencils, usage of the LODI or LZG BC leads to a significantly smaller deviation from the reference simulation than the ZG BC. Reflections due to the BC travel through the bulk and are absorbed by the NRBC at the opposite site of the domain, shrinking the errors further after about 250 time steps. In contrast, the constant errors for the ZG scheme correspond to a significantly altered steady state when compared to the reference simulation.

before being absorbed by the NRBC at the respective other end, causing both e_ρ and e_{u_x} to drop two orders of magnitude after around 250 time steps. The behavior of the ZG scheme is completely different. Here, both errors saturate at a level several order of magnitude larger than for the other schemes, leading to a steady state significantly different from the reference solution.

For comparison, we show the results of the benchmark simulated using the D2Q9 stencil. Note that in this case the LZG and LODI schemes coincide by construction. Remarkably, the error level is approximately the same as for the D2Q17 model, showing that our implementation does not introduce any extra source of inaccuracy despite the treatment of multiple layers of boundary nodes.

In Fig. 3 we show the time evolution of the error for a selected observation point (OP), taken in the proximity of the right boundary and having coordinates $\mathrm{OP} = (L_x - 5, \frac{L_y}{2})$. We track the time evolution of macroscopic quantities $Z \in \{\rho, u_x\}$ in OP, showing the deviation

$$\Delta Z = |Z - Z^{\mathrm{ref}}|$$

from the macroscopic values of the reference simulation.

Again, we observe very similar results for LODI and LZG. Small spikes can be seen whenever the original wave, or the reflection from the left boundary, passes through the

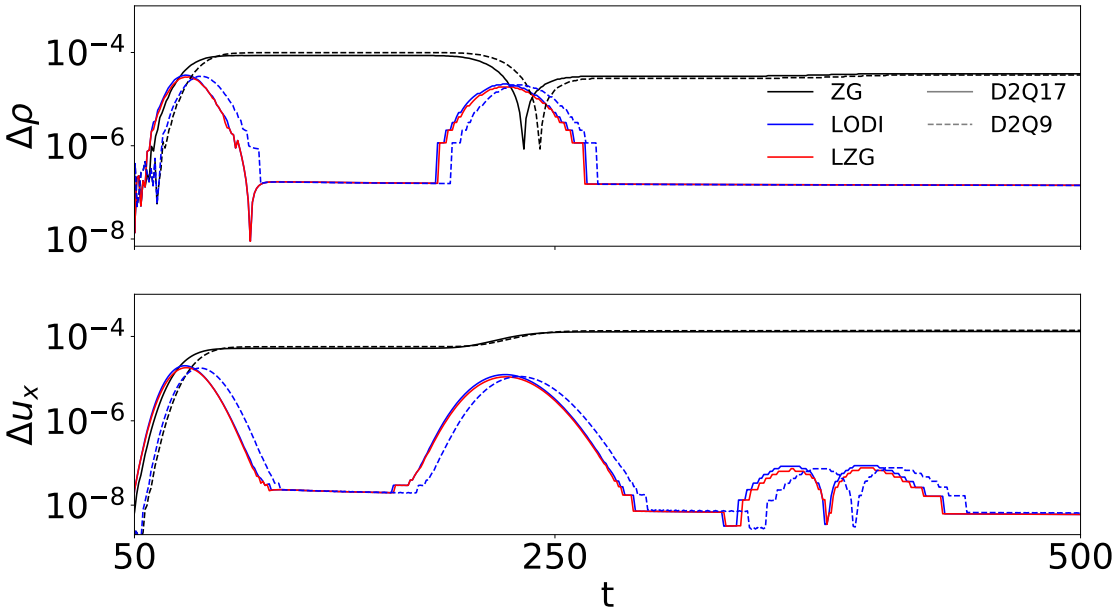

Figure 3: Deviation of macroscopic density and velocity in the point OP $=(L_x-5,\frac{L_y}{2})$ from reference values computed on a large periodic grid. The initial peak corresponds to the original wave boundary interaction. A second slightly smaller peak is observed when a wave created from interaction with the left boundary has traveled through OP. A third significantly smaller peak is observed in the velocity, where reflections apparently are not as effectively reduced as in the density. The deviations approach a steady level and remain stationary after 500 time steps (not shown). Solid (dashed) lines correspond to simulations using the D2Q17 (D2Q9) velocity stencil.

observation point. For the ZG BC, the boundary treatment of the initial pulse causes an overshoot with respect to the reference density in the first few iterations. Then, the traveling wave from the left boundary reflection causes the density at OP to drop below the reference level. This gives the observed v-shape structure at around 250 time steps. Consistent with the discussion of Fig. 2, the deviation remains orders of magnitude larger than with LODI or LZG.

4.2 Vortex propagation

We now consider a second benchmark, simulating the propagation of a vortex, hence a fully bi-dimensional dynamic. We work on a grid of size $L_x\times L_y=150\times 150$ and setting the numerical viscosity to $\nu=0.1$ in lattice units.

The initial conditions are given by a uniform background velocity $\mathbf{u_0}=(\mathrm{Ma}\cdot c_s,0)^\top$, with Mach number $\mathrm{Ma}=0.1$, and with a perturbation defined within a disk centered around a node of coordinates $(\frac{L_x}{2}+K,\frac{L_y}{2})$ and of radius r. Moreover, we the background

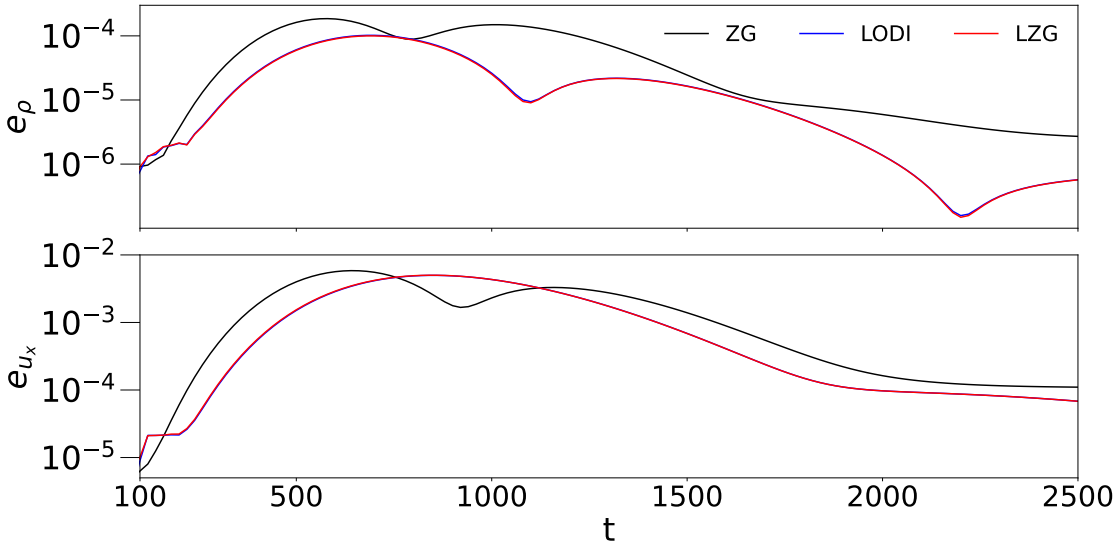

Figure 4: Relative L^2-errors in density and streamwise velocity for the vortex propagation benchmark with respect to the reference simulation. The accuracy of the LODI and LZG BC are comparable, with errors in the same order of magnitude. The ZG scheme produces smaller errors in the streamwise velocity between 800 and 1100 time steps.

density is uniform and set to unity. To summarize:

$$\rho(x,y)=1,$$
$$\mathbf{u}(x,y)=\mathbf{u_0}+\begin{cases}0, & \text{if } (\hat{x}-\hat{x}_0)^2+\hat{y}^2\geq r^2,\\ \mathbf{v}(\hat{x},\hat{y}), & \text{otherwise,}\end{cases} \qquad v(x,y)=\frac{5\text{Ma}}{2}2^{-\frac{x^2+y^2}{b^2}}\begin{pmatrix}y\\-x\end{pmatrix}c_s,$$

with the following parameters:

$$\hat{x}_0=K\frac{2}{L_x-1}, \quad \hat{x}=\frac{2x}{L_x-1}-1, \quad \hat{y}=\frac{2y}{L_y-1}-1, \quad b=0.15, \quad K=20, \quad r=0.7. \tag{4.1}$$

In this benchmark, all boundaries and corners are equipped with a NRBC.

In Fig. 4, we show the time evolution of the L^2-errors e_ρ and e_{u_x}. Although the LODI BC outperforms on average the ZG, in this second benchmark the differences between them are very much reduced, especially in comparison with the results of the 1D benchmark presented in the previous section. The loss of advantage in this 2D setting is somewhat expected, since all information about the now relevant parallel derivatives is discarded when working in the LODI framework. We take as positive the fact that LODI and LZG produce very similar results, even in this second benchmark.

While Fig. 4 shows the time evolution of the integrated relative error over the entire domain, it is instructive to compare the different implementations from another perspective. In Fig. 5 and Fig. 6, we show the density and the streamwise velocity profiles of the

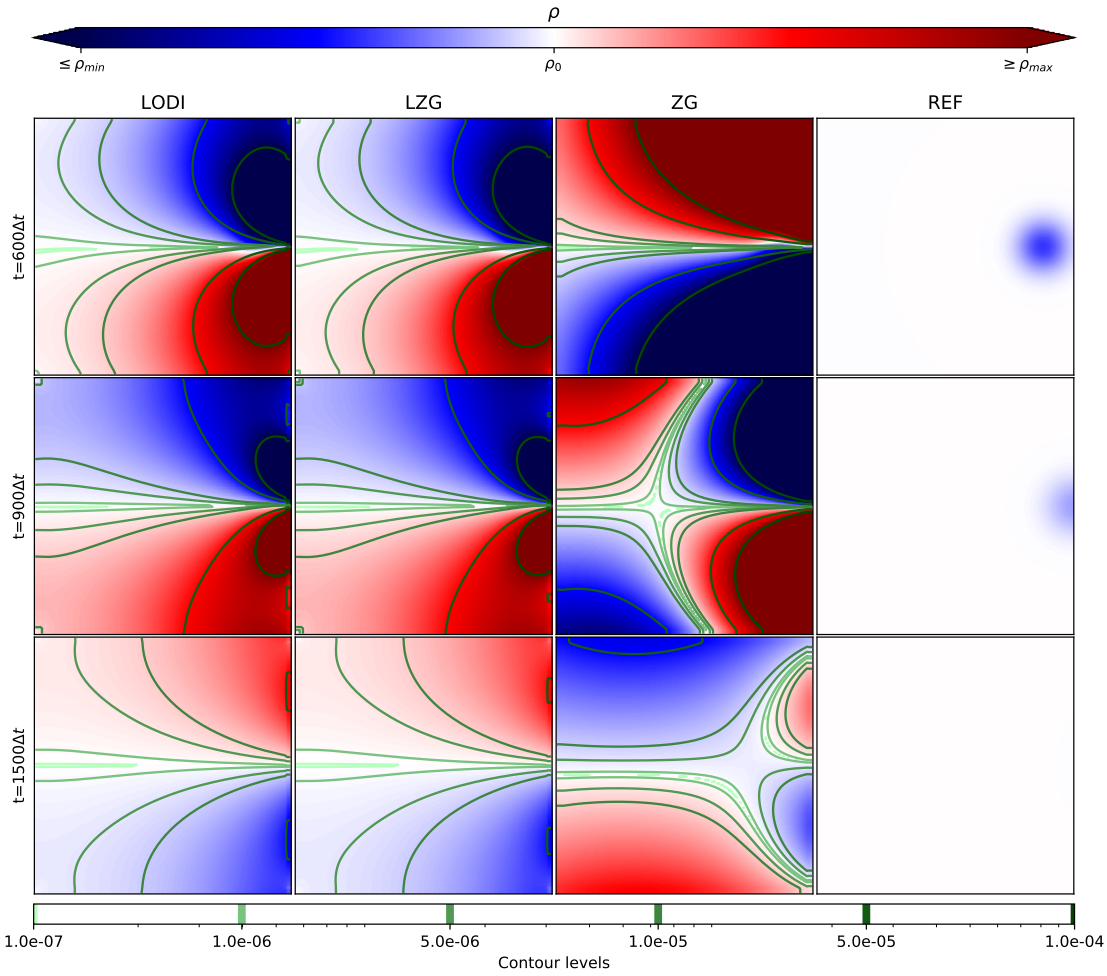

Figure 5: First to third column: Snapshots of density profiles ρ with contours of pointwise relative error with respect to the reference simulation for the considered BC. Last column: Corresponding snapshot of ρ^{ref}. The upper colorbar for ρ is capped at $\rho_{\text{max,min}} = \rho_0 \pm \epsilon$, where $\rho_0 = 1$, $\epsilon = 1 \cdot 10^{-4}$.

flow at a few selected time steps, comparing the results produced by the different BCs against the reference solution. We have also overlaid iso-contour lines giving a visual representation of six selected values of the relative error.

The first, second and third rows of panels represent an early, medium and late stage of the vortex boundary interaction, respectively.

We observe that in the LODI scheme, the error streamlines are mostly distributed in the proximity of the right boundary, indicating that the bulk dynamics are less affected than with the ZG BC. One notable exception occurs in the streamwise velocity after 900 time steps. Here, the profile obtained with ZG is closer to the reference profile. Indeed,

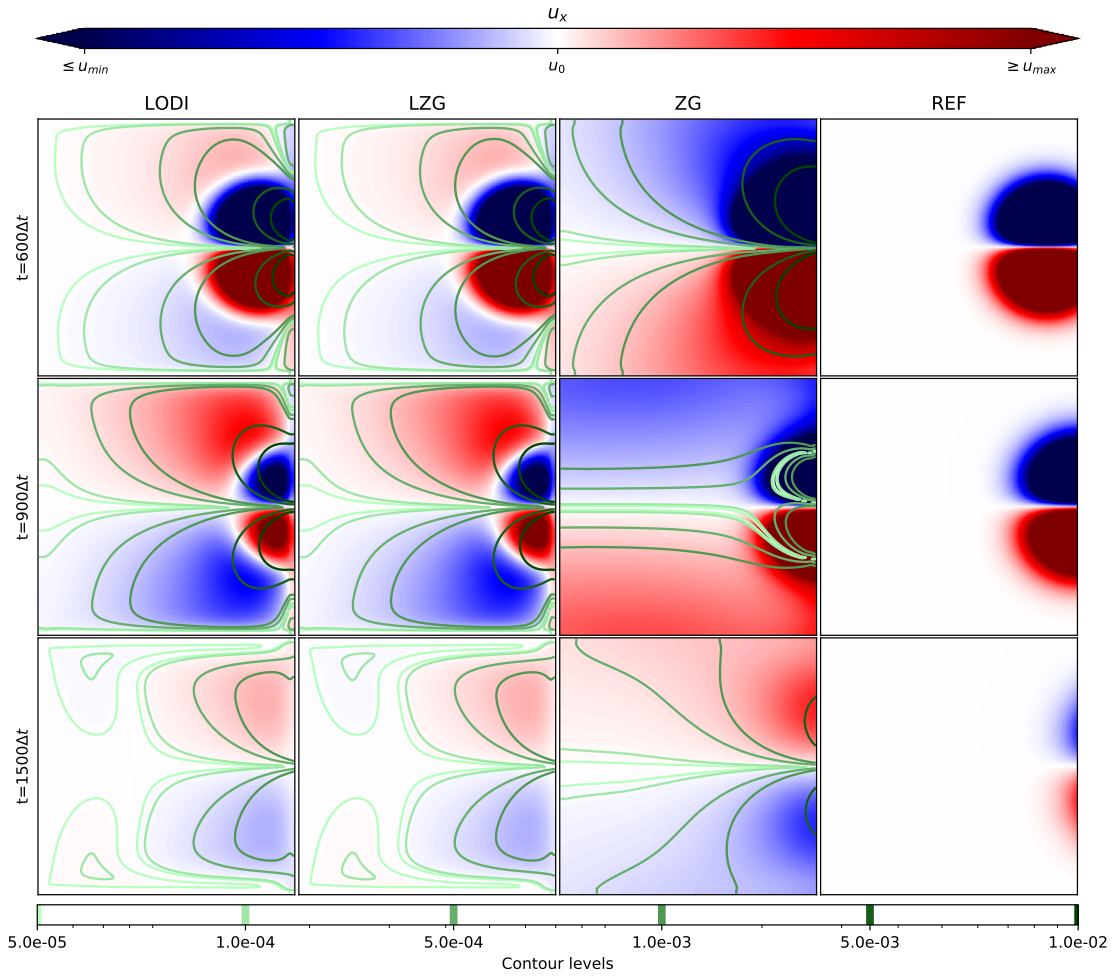

Figure 6: First to third column: Snapshots of streamwise velocity profiles u_x with contours of pointwise relative error with respect to the reference simulation for the considered NRBC. Last column: Corresponding snapshot of u_x^{ref}. The upper colorbar for u_x is capped at $u_{\text{max,min}} = u_0 \pm \epsilon$, where $u_0 = \text{Ma} \cdot c_s$, $\epsilon = 5 \cdot 10^{-4}$.

from Fig. 4, we see that e_{u_x} is lower for the ZG scheme and close to its maximum for the LODI BC. However, we observe that the main contribution to e_{u_x} lies in the vortex boundary interaction: The height of the vortex is notably smaller with the LODI BC than with the ZG BC, indicating that the boundary absorbs the velocity perturbation more efficiently. However, this lack of accuracy in modeling the boundary interaction is not a problem in practice, since the main point of using artificial boundaries is not polluting the bulk dynamics. It is also notable that the macroscopic quantities deviation from their reference counterpart often has a different sign in the ZG BC than with LODI.

5 Conclusion

In this work, we have extended and applied a characteristic BC to multi-speed velocity stencils that exhibit multiple layers of boundary nodes. We have implemented this technique within two schemes: LODI and LZG scheme.

In the LODI scheme, the characteristic analysis is conducted layer per layer. In the LZG scheme, this is only done once in the innermost layer of the boundary and the resulting macroscopic target values are posed in each layer using an equilibrium BC. This more unified treatment considerably simplifies the task of specifying a BC for multi-speed velocity stencils. We assessed the accuracy of both schemes using two numerical benchmarks, namely a mono-dimensional flow triggered by a density perturbation, and the fully bi-dimensional flow of a traveling vortex. The numerical results show that the advantages offered by non-reflecting BC over a simple zero gradient BC, observed in previous works using the D2Q9 stencil, are retained when extending to multi-speed velocity stencils. Moreover, the simplified LZG implementation offers a level of accuracy very similar to the LODI scheme.

On the other hand, the gains in accuracy are reduced for fully bi-dimensional flows, since the parallel derivatives are discarded in the LODI framework. Starting from this observation, future research will aim at incorporating the information loss in the transversal direction into a modified version of the LODI scheme. Furthermore, the reincorporation of viscosity effects shall also be investigated, as it might further increase the accuracy of characteristic multi-speed boundary conditions.

Appendix A: Pseudocode for LODI and LZG boundary condition

In this Appendix section we provide further details on the implementation of the boundary conditions presented in Section 3. We work on a rectangular domain of size $L_x \times L_y$ and consider as an example a right boundary (see Fig. 1). Algorithm 1 lists the computational steps required for the calculation of the macroscopic values at the boundary nodes using the LODI and LZG boundary conditions described in the main text. These values are then used to define the missing particle distribution functions at the boundary layer in the LBM simulation using a Dirichlet BC.

We remark that the results reported in Section 4 have been obtained prescribing the equilibrium (2.2) for the Dirichlet BC, and a forward Euler scheme for the time discretization of the LODI-ODE (3.5). More advanced / higher-order schemes may be taken into consideration as well. However, numerical experiments with a second order time approximation and different Dirichlet BC yielded negligible differences in the benchmarks taken into consideration in this work.

Algorithm 1: Pseudo-code for a right boundary (see Fig. 1) using LODI and LZG BC. In the D2Q17 model adopted in this work, the maximum displacement is $M=3$. Here, LZG is a boolean flag variable indicating whether LODI or LZG is applied.

for $y \leftarrow 1$ **to** L_y **do**
  for $x \leftarrow L_x - M + 1$ **to** L_x **do**
    $\mathbf{x} = (x,y)^\top$
    /* compute $\frac{\partial Z}{\partial x}$ using (3.6) and (3.7) for $Z \in \{\rho, \mathbf{u}\}$ */
    if $\left((x == L_x) \;||\; LZG\right)$ **then**
      $\frac{\partial Z(\mathbf{x},t)}{\partial x} \approx -\frac{1}{2}\left(-3Z(\mathbf{x},t) + 4Z(\mathbf{x}-\mathbf{e}_x,t) - Z(\mathbf{x}-2\mathbf{e}_x,t)\right)$
    else
      $\frac{\partial Z(\mathbf{x},t)}{\partial x} \approx \frac{1}{2}\left(Z(\mathbf{x}+\mathbf{e}_x,t) - Z(\mathbf{x}-\mathbf{e}_x,t)\right)$
    end
    /* compute $\mathcal{L}_x$ using (3.3) */
    $\mathcal{L}_{x,1} = (u_x - c_s)(c_s^2 \frac{\partial \rho}{\partial x} - c_s \rho \frac{\partial u_x}{\partial x})$
    $\mathcal{L}_{x,2} = u_x \frac{\partial u_y}{\partial x}$
    $\mathcal{L}_{x,3} = (u_x + c_s)(c_s^2 \frac{\partial \rho}{\partial x} + c_s \rho \frac{\partial u_x}{\partial x})$
    /* compute $\bar{\mathcal{L}}_x$ using (3.4), set incoming amplitudes to zero */
    $\bar{\mathcal{L}}_{x,1} = \left((u_x - c_s < 0)\;?\;0 : \mathcal{L}_{x,1}\right)$
    $\bar{\mathcal{L}}_{x,2} = \left((u_x \quad\;\; < 0)\;?\;0 : \mathcal{L}_{x,2}\right)$
    $\bar{\mathcal{L}}_{x,3} = \left((u_x + c_s < 0)\;?\;0 : \mathcal{L}_{x,3}\right)$
    /* solve (3.5) with explicit Euler for target values $U = (\rho, \mathbf{u})^\top$ with lattice time step $\Delta t = 1$ and macroscopic values U_{-1} from the previous time step */
    $U = -S^{-1}\bar{\mathcal{L}}_x + \Delta t U_{-1}$
    /* apply equilibrium (2.2) as boundary condition: */
    $f_i(\mathbf{x},t) = f_i^{\mathrm{eq}}(\rho,\mathbf{u}), \quad i = 1,\ldots,q$
    if *LZG* **then**
      break
    end
  end
  if *LZG* **then**
    /* apply zero gradient: */
    for $j \leftarrow 1$ **to** $M-1$ **do**
      $\hat{\mathbf{x}} = (x+j, y)^\top$
      $f_i(\hat{\mathbf{x}},t) = f_i(\mathbf{x},t) \quad i = 1,\ldots,q$
    end
  end
end

References

[1] S. Succi, The Lattice Boltzmann Equation: For Complex States of Flowing Matter, OUP Oxford, 2018. doi:10.1093/oso/9780199592357.001.0001.

[2] S. Succi, Lattice Boltzmann beyond Navier-Stokes: Where do we stand?, in: AIP Conference Proceedings, Author(s), 2016. doi:10.1063/1.4967538.

[3] P. C. Philippi, L. A. Hegele, L. O. E. dos Santos, R. Surmas, From the continuous to the lattice Boltzmann equation: The discretization problem and thermal models, Physical Review E 73 (5) (May 2006). doi:10.1103/physreve.73.056702.

[4] S. S. Chikatamarla, I. V. Karlin, Lattices for the lattice Boltzmann method, Phys. Rev. E 79 (2009) 046701. doi:10.1103/PhysRevE.79.046701.

[5] X. Shan, The mathematical structure of the lattices of the lattice Boltzmann method, Journal of Computational Science 17 (2016) 475–481. doi:10.1016/j.jocs.2016.03.002.

[6] A. Scagliarini, L. Biferale, M. Sbragaglia, K. Sugiyama, F. Toschi, Lattice Boltzmann methods for thermal flows: Continuum limit and applications to compressible Rayleigh-Taylor systems, Physics of Fluids 22 (5) (2010) 055101. doi:10.1063/1.3392774.

[7] N. Frapolli, S. S. Chikatamarla, I. V. Karlin, Multispeed entropic lattice Boltzmann model for thermal flows, Physical Review E 90 (4) (Oct. 2014). doi:10.1103/physreve.90.043306.

[8] N. G. Kallikounis, B. Dorschner, I. V. Karlin, Multiscale semi-Lagrangian lattice Boltzmann method, Phys. Rev. E 103 (2021) 063305. doi:10.1103/PhysRevE.103.063305.

[9] V. E. Ambruş, V. Sofonea, High-order thermal lattice Boltzmann models derived by means of Gauss quadrature in the spherical coordinate system, Phys. Rev. E 86 (2012) 016708. doi:10.1103/PhysRevE.86.016708.

[10] O. Ilyin, Gaussian lattice Boltzmann method and its applications to rarefied flows, Physics of Fluids 32 (1) (2020) 012007. doi:10.1063/1.5126306.

[11] Y. Shi, L. Wu, X. Shan, Accuracy of high-order lattice Boltzmann method for non-equilibrium gas flow, Journal of Fluid Mechanics 907 (2021) A25. doi:10.1017/jfm.2020.813.

[12] M. Mendoza, S. Succi, H. J. Herrmann, Flow through randomly curved manifolds, Scientific reports 3 (1) (2013) 1–6. doi:10.1038/srep03106.

[13] R. C. Coelho, M. M. Doria, Lattice Boltzmann method for semiclassical fluids, Computers & Fluids 165 (2018) 144–159. doi:https://doi.org/10.1016/j.compfluid.2018.01.019.

[14] A. Gabbana, D. Simeoni, S. Succi, R. Tripiccione, Relativistic lattice Boltzmann methods: Theory and applications, Physics Reports 863 (2020) 1–63. doi:10.1016/j.physrep.2020.03.004.

[15] H. Lee, S. Bawazeer, A. Mohamad, Boundary conditions for lattice Boltzmann method with multispeed lattices, Computers & Fluids 162 (2018) 152–159. doi:10.1016/j.compfluid.2017.12.011.

[16] F. Klass, A. Gabbana, A. Bartel, A non-equilibrium bounce-back boundary condition for thermal multispeed LBM, Journal of Computational Science 53 (2021) 101364. doi:10.1016/j.jocs.2021.101364.

[17] J. Meng, Y. Zhang, Diffuse reflection boundary condition for high-order lattice Boltzmann models with streaming–collision mechanism, Journal of Computational Physics 258 (2014) 601–612. doi:10.1016/j.jcp.2013.10.057.

[18] A. Najafi-Yazdi, L. Mongeau, An absorbing boundary condition for the lattice Boltzmann method based on the perfectly matched layer, Computers & Fluids 68 (2012) 203–218. doi:10.1016/j.compfluid.2012.07.017.

[19] D. Heubes, A. Bartel, M. Ehrhardt, Discrete Artificial Boundary Conditions for the Lattice

Boltzmann Method in 2D, ESAIM: Proceedings and Surveys 52 (2015) 47–65. doi:10.1051/proc/201552003.

[20] S. Izquierdo, N. Fueyo, Characteristic nonreflecting boundary conditions for open boundaries in lattice Boltzmann methods, Physical Review E 78 (4) (Oct. 2008). doi:10.1103/physreve.78.046707.

[21] G. Hedstrom, Nonreflecting boundary conditions for nonlinear hyperbolic systems, Journal of Computational Physics 30 (2) (1979) 222–237. doi:10.1016/0021-9991(79)90100-1.

[22] K. W. Thompson, Time dependent boundary conditions for hyperbolic systems, Journal of Computational Physics 68 (1) (1987) 1–24. doi:10.1016/0021-9991(87)90041-6.

[23] T. Poinsot, S. Lelef, Boundary conditions for direct simulations of compressible viscous flows, Journal of Computational Physics 101 (1) (1992) 104–129. doi:10.1016/0021-9991(92)90046-2.

[24] X. Shan, General solution of lattices for Cartesian lattice Bhatanagar-Gross-Krook models, Phys. Rev. E 81 (2010) 036702. doi:10.1103/PhysRevE.81.036702.

[25] P. L. Bhatnagar, E. P. Gross, M. Krook, A Model for Collision Processes in Gases. Amplitude Processes in Charged and Neutral One-Component Systems, Phys. Rev. 94 (3) (1954) 511–525. doi:10.1103/PhysRev.94.511.

[26] X. Shan, X.-F. Yuan, H. Chen, Kinetic theory representation of hydrodynamics: A way beyond the Navier-Stokes equation, Journal of Fluid Mechanics 550 (2006) 413–441. doi:10.1017/S0022112005008153.

[27] S. Chapman, T. G. Cowling, The Mathematical Theory of Non-Uniform Gases, 3rd. ed., Cambridge University Press, 197. doi:10.1119/1.1942035.

[28] D. Heubes, A. Bartel, M. Ehrhardt, Characteristic boundary conditions in the lattice Boltzmann method for fluid and gas dynamics, Journal of Computational and Applied Mathematics 262 (2014) 51–61. doi:10.1016/j.cam.2013.09.019.

[29] N. Jung, H. W. Seo, C. S. Yoo, Two-dimensional characteristic boundary conditions for open boundaries in the lattice Boltzmann methods, Journal of Computational Physics 302 (2015) 191–199. doi:10.1016/j.jcp.2015.08.044.

[30] D. Heubes, Artificial Boundary Conditions in the Lattice Boltzmann Method, Dissertation, Bergische Universität Wuppertal (2016).
URL http://elpub.bib.uni-wuppertal.de/servlets/DerivateServlet/Derivate-6425/dc1702.pdf